



# The combined effect of fractures and mineral content on coal hydromechanical response

Adelina Lv<sup>1</sup> · Mojtaba Bahaaddini<sup>2,3</sup> · Hossein Masoumi<sup>4</sup> · Hamid Roshan<sup>1</sup>

Received: 25 October 2021 / Accepted: 26 March 2022 / Published online: 6 April 2022  
© The Author(s) 2022

## Abstract

The hydromechanical behaviour of fractured coal is a complex function of interaction between coal bulk and fracture deformation driven by fluid pressure and external stress. Despite the research studies conducted to date, the combined effect of mineral content and fracture structure on hydromechanical behaviour of sorptive fractured coal remains unexplored. To study this combined effect, we performed a series of X-ray computed tomography (XRCT) imaging on a range of coal specimens with non-sorbing (helium) and sorbing (CO<sub>2</sub>) gases at different effective stress paths using a newly developed X-ray transparent triaxial system. The compressibility of system components was obtained from processed 3D XRCT images which were used to interpret the results. The results of this study show that coal matrix/solid compressibility has a positive nonlinear relation with mineral content irrespective of mineral type. Effective stress coefficient is also a strong function of both mineral content and fracture porosity. Furthermore, the increase in mineral content leads to less fracture opening by an increase in helium pressure. Interestingly, the effect of mineral content on the bulk strength of coal is more significant than the effect of fracture porosity. Finally, coal with more open fractures shows less bulk swelling by gas adsorption under external stress due to damping effect of fracture volume on developed internal volumetric swelling strain.

**Keywords** Hydromechanical response · Fractures · Mineral content · Compressibility · Porosity · Gas adsorption

## Abbreviations

$\sigma'$	Effective stress
$\sigma$	Total stress
$\Phi$	Porosity
$\varepsilon_b$	Volumetric strain of bulk
$\varepsilon_f$	Volumetric strain of fracture
$\gamma$	Effective stress coefficient (ESC)
$C_{bc}$	Bulk volume compressibility, under constant pore pressure
$C_{bp}$	Bulk volume compressibility, under constant confining stress

$C_{fc}$	Fracture volume compressibility, under constant pore pressure
$C_{fp}$	Fracture volume compressibility, under constant confining stress
$C_s$	Solid compressibility
$C_\phi$	Unjacketed fracture compressibility
$K$	Bulk modulus
$K_f$	Bulk modulus of fractures
$K_s$	Solid bulk modulus
$p$	Pore pressure
$P_d$	Differential pressure between confinement and pore pressure
$V$	Bulk volume
$V_f$	Fracture volume
$V_s$	Solid volume

✉ Hamid Roshan  
h.roshan@unsw.edu.au

<sup>1</sup> School of Minerals and Energy Resources Engineering, University of New South Wales, Sydney, NSW 2052, Australia

<sup>2</sup> School of Mining Engineering, College of Engineering, University of Tehran, Tehran, Iran

<sup>3</sup> Shahid Bahonar University of Kerman, Kerman, Iran

<sup>4</sup> Department of Civil Engineering, Monash University, Melbourne, VIC 3800, Australia

## Introduction

The enhanced coalbed methane recovery and CO<sub>2</sub> storage in coal seams has gained a broad interest in recent decades (Detheridge et al. 2019; Karacan et al. 2011; Shi and Durucan 2005). In the coalbed methane recovery, the

pressure-driven fluid flow often combined with hydraulic fracturing and  $N_2$ — $CO_2$  injection is used to produce the methane. The geological storage of carbon in coalbed seams can be also achieved through this technique (Bachu 2003; Gou et al. 2021). The  $CO_2$  injection for enhanced coalbed methane leads to swelling of the coal matrix which can in turn reduce the coal permeability significantly (Bertrand et al. 2019; Li and Fang 2014). The interaction between bulk of solid with fractures and fluid constitutes is thus of critical importance during coalbed methane production. Such interaction is complex, especially when sorbing gas is involved. Amongst different aspects of these interactions, the hydromechanical response of fractured coal in the presence of non-sorbing and sorbing gases needs special attention. The study of hydromechanical response of geomaterials goes back to the work of Biot (1941) and Terzaghi (1943). Their theories have been extensively used in rock and soil mechanics for analysis of the rock hydromechanical behaviour. Following Biot's work, poroelastic behaviour of geomaterials was further explored by many researchers (Detournay and Cheng 1993; Gassmann 1951; Rice and Cleary 1976; Zimmerman et al. 1986).

The Biot linear poroelasticity was defined for porous media consisting of grains and pores (Lv et al. 2019). The coal structure, however, contains fractures with micrometers aperture (cleats) and matrix that contains a range of pores with majority sitting in nanometer scale. In a recent study, Lv et al. (2021a) showed that the Biot poroelasticity can be used for fractured coal considering matrix as the solid and fractures as void constitute. Recent studies (Lv et al. 2021b, 2022) also indicated that coal fractures are highly sensitive to external stress and pore pressure even for stresses lower than 1 MPa, while matrix micropores require much higher level of stress to deform (above 10 MPa). When sorbing gas is considered, the gas stays at bulk condition in the fractures, while it is mostly adsorbed in matrix micropores; thus, hydromechanical response (no sorption involved) is dictated by the fractures' behaviour which depends on stress and pore pressure of the system.

Hydromechanical responses of coal especially from porosity and bulk volume perspective have been studied in the literature (Cheng et al. 2021; Tan et al. 2019; Wang et al. 2020; Zhang et al. 2019) concluding that the higher porosity leads to higher compressibility of the coal bulk. For instance, Shao et al. (2018) showed that the matrix compressibility has a strong correlation with porosity and mineral content in coal. Golsanami et al. (2019) differentiated the fracture porosity from matrix pores and studied its relation to bulk and Young's modulus calculated from acoustic velocities. The impact of mineral matter on hydromechanical responses of coal can be attributed to mineral content, mineralogical composition and morphology (Ahamed et al. 2019). The effect of mineral content and composition

on mechanical properties of coal has been investigated in the literature showing that the high-density minerals can stiffen the coal matrix and significantly decrease its bulk compressibility. In an early study, Barbour and Ko (1979) investigated the effect of carbonate and clay contents on the Young's modulus of coal and found that an increase in carbonate content of coal results in an increase in Young's modulus while the clay content has an opposite effect. Guo et al. (2014) tested 21 coal samples of different ranks and concluded that porosity and organic matter content were positively correlated to the matrix compressibility, except for high-volatile group with low minerals content. This important finding from experimental observation was also confirmed by Wetzel et al. (2018) through simulation on synthetic digital rocks, where a positive correlation between calcite content and the bulk modulus was found. Cai et al. (2018) concluded that clay mineral content shows negative exponential correlation to matrix compressibility from the obtained experimental results of coal samples with mineral contents less than 20%. Following these experimental results, Song and Liu (2020) used carbonate solution to improve the coal strength. In addition, Miao et al. (2020) performed hydromechanical experiments on different coal samples leading to similar conclusion that the coal matrix compressibility decreases with an increase in the minerals content. The possible effect of mineral structure on coal bulk compressibility, however, has not been fully understood due to limitations of traditional methods in tracking mineral structures, especially when the mineral content is low. To investigate the coal mechanical properties through morphological characteristics, non-destructive methods such as X-ray Computed Tomography (XRCT), Scanning Electron Microscopy (SEM), and ultrasonic transmission, are used.

In particular, the rapid development of laboratory XRCT over the past decades has enabled studying different processes in coal (Mathews et al. 2017). The XRCT is occasionally combined with other methods such as SEM (Gupta 2007) to attain more detailed information. This information is generally used to model permeability (Liu et al. 2020; Ramandi et al. 2021; Wang et al. 2019b; Zhao et al. 2018; Zhu et al. 2021), sorption effect (Karacan and Okandan 2001; Pirzada et al. 2018; Shi et al. 2020) and mechanical deformation of coal (Dong et al. 2021; Lv et al. 2019; Stappen et al. 2019; Wang et al. 2021; Zhao et al. 2019). To investigate the mechanical deformation and fluid transport in porous media, XRCT images are used in simulation exercises (Blaheta et al. 2015; Chen et al. 2019; Roslin et al. 2019; Wang et al. 2019a; Wei et al. 2021; Zhang et al. 2017; Zhao et al. 2019). An example of recent hydro-mechanical simulation on XRCT images is the development of a novel method to calculate Biot's coefficient in a granular media (2021). Using image segmentation, fractures, coal organic matter and mineral contents can be differentiated to

investigate their interactions with each other. For example, Zhang et al. (2018) reported that Young’s modulus of coal is highly influenced by the mineral content through XRCT and acoustic measurements. Li et al. (2020) observed a noticeable difference between mechanical properties of coal matrix and mineral through 2D and 3D XRCT image analysis.

Sorption effect is another distinct natural behaviour of coal; the sorption capacity is closely related to coal composition, especially carbon content and micro-structure influencing gas accessibility (Cheng et al. 2017; Crosdale et al. 1998; Hou et al. 2017). Due to microscopic structure of carbon molecules, organic matter content has a positive effect on the sorption capacity (Chalmers and Bustin 2007; Mastalerz et al. 2004; Meng and Liu 2018). The mineral matters, on the other hand, have a negative impact on the sorption capacity (Laxminarayana and Crosdale 1999) due to their low adsorption capacity compared to organic matters (Clarkson and Bustin 1996) although minerals like clay can still contribute to sorption capacity (Deng et al. 2015). Pone et al. (2009) suggested that mineral distribution can influence the connectivity of the microstructures and continuity of the pore networks thus affecting gas sorption process. It is clear from above discussion that investigating the combined effect of mineral content and fractures on hydromechanical response of coal requires hydromechanical testing coupled with methods such as XRCT.

In this study, we therefore employed micro-XRCT ( $\mu$ CT) technique to investigate the hydromechanical response of different coal samples though analysing bulk and fracture volumes with non-sorbing and sorbing gases using a newly designed X-ray transparent triaxial system (Roshan et al. 2019a). To investigate the contribution of different mineral contents on hydromechanical behaviour of coals, images were segmented into fracture, organic matter, and mineral domains and the volumetric strain of the bulk and fractures were extracted to calculate the compressibilities of fracture and matrix as well as the effective stress coefficient. The imaging results were then compared with a measured effective stress coefficient of one of the coal specimens to assess its validity. The obtained compressibilities of fracture and matrix as well as the effective stress coefficient were then linked to mineral content and fracture porosity. The XRCT imaging was also performed with an adsorption test to investigate the effect of adsorption on the hydromechanical process.

### Characterization of hydromechanical properties

In order to systematically analyse the effect of mineral content and structure on hydromechanical response of fractured coals, we follow the definition of compressibility of the porous rock constitutes introduced by Zimmerman et al. (1986). This

methodology allows us to link the mineral content to different compressibilities of the fractured coal. Knowing that the fractures are much more compressible than micropores in the coal matrix, especially under a low level of external stress, and by analogy to a pore-solid system, the volume of the bulk of fractured coal ( $V_b$ ) is defined as sum of the fracture volume,  $V_f$  and matrix volume,  $V_m$  including solids and its micropores.

$$V_b = V_f + V_m \tag{1}$$

Fracture porosity,  $\phi_f$  is then defined as the ratio of fracture volume to bulk volume:

$$\phi_f = V_f/V_b \tag{2}$$

Having two phases (matrix and fracture), the system compressibility functions for the fractured coal are defined according to Zimmerman et al. (1986) for porous rock (compressive stress and strain are assumed positive) including:

- (a) bulk compressibility at different boundary conditions (BCs):

$$C_{bc} = -\frac{1}{V_b} \left( \frac{\partial V_b}{\partial \sigma} \right)_{\Delta p=0} \quad C_{bp} = \frac{1}{V_b} \left( \frac{\partial V_b}{\partial p} \right)_{\Delta \sigma=0} \tag{3}$$

where  $\sigma$  and  $p$  are the total stress and pore pressure, respectively. Also  $C_{bc}$  and  $C_{bp}$  are bulk compressibilities measured at constant pore pressure and constant external stress, respectively.

- (b) fracture compressibility at different BCs:

$$C_{fc} = -\frac{1}{V_f} \left( \frac{\partial V_f}{\partial \sigma} \right)_{\Delta p=0} \quad C_{fp} = \frac{1}{V_f} \left( \frac{\partial V_f}{\partial p} \right)_{\Delta \sigma=0} \tag{4}$$

where  $C_{fc}$  and  $C_{fp}$  are the fracture compressibilities measured at constant pore pressure and constant external stress, respectively. In addition to above compressibilities of system components, the solid (matrix) compressibility,  $C_s$  is also defined as:

$$C_s = -\frac{1}{V_b} \left( \frac{\partial V_b}{\partial \sigma} \right)_{\Delta \sigma = \Delta p \text{ or } P_d} \tag{5}$$

In a laboratory measurement,  $C_s$  is measured from an unjacketed test where the differential pressure  $P_d$  is kept constant.  $P_d$  is defined as the difference between the total stress and the pore pressure.

Biot’s concept of effective stress law (Biot 1941) defines the effective stress,  $\sigma'$  of a porous medium by relating the total stress,  $\sigma$  to pore pressure,  $p$  through the effective stress coefficient,  $\gamma$  (or ESC):

$$\sigma' = \sigma - \gamma p \tag{6}$$

While the Biot poroelasticity was defined around solid constitute and pores, recent study by Lv et al. (2021a)

showed that it can be used for fractured coal, where coal matrix is considered as the solid constitute and fractures as voids. The  $\gamma$  can be measured using jacketed-unjacketed test (Biot and Willis 1957; Geertsma 1957; Skempton 1961). In Eq. (3),  $C_{bp}$  is measured from a hydrostatic compression on a jacketed specimen under  $\Delta p = 0$ .  $C_s$  is measured from a hydrostatic compression under  $\Delta P_d = 0$  as in Eq. (5). The  $\gamma$  then describes the effect of void volume on the bulk deformation which ranges from 0 to 1.

$$\gamma = 1 - \frac{C_s}{C_{bp}} \quad (7)$$

Another way of measuring the  $\gamma$  is through a hydrostatic compressive test under  $\Delta p = 0$ . From Eq. (8),  $\gamma$  is determined by the change in fracture volume,  $\Delta V_f$  and bulk volume,  $\Delta V_b$  leading to (Franquet and Abass 1999):

$$\gamma = \frac{\Delta V_f}{\Delta V_b} \quad (8)$$

## Experimental methodology

### Sample preparation and characteristics

All coal samples used in this study were collected from different boreholes from a coal seam in Sydney Basin, New South Wales, Australia (Zhao 2012). Before coring, a layer of resin was applied on the surface of coal samples allowing at least one day for plasticising. Then, a half-inch (12.7 mm) coring bit was used to obtain specimens with a diameter of about 12.5 mm. The coal specimens were then cut into a length of approximately 2 times of the diameter (between 19 to 28 mm depending on the brittleness of the coal sample). Finally, specimens were evacuated in the oven at 105° Celsius for at least 2 days to remove any moisture.

Six coal specimens labelled as SY1 (one specimen), SY2 (one specimen) and SY3 (four specimens labelled as SY3-1 to SY3-4) with varying fracture porosity and mineral content were used for the analysis. Fracture porosity refers to the ratio of fracture volume per bulk volume of the specimen and mineral content refers to minerals volume per bulk volume of the specimen. The SY2 specimen had the lowest mineral content of 2.49% volume ratio, followed by SY1 with 8.76%. The SY3 specimens had a high mineral content of average above 30% showing a distinct minerals content difference with SY1 and SY2. In addition, the unconfined fracture porosity was around 0.8% and 0.7% for SY1 and SY2, respectively, whereas SY3 specimens had different fracture porosity ranging from approximately 0.3% to 0.8%. Specimens with different fracture porosity and mineral content were used for different tests that will be further explained in

the experimental methodology. The leftover powder from the samples was used for X-ray diffraction to identify the mineral composition of each category (SY1 to SY3).

### X-ray diffraction

X-ray diffraction (XRD) was carried out on three coal samples from each category. Samples were measured in PANalytical MPD Powder diffractometer, with Cu X-ray source, at 45 kV and 40 mA X-Ray generation condition. XRD results of three samples are summarised in Table 1 showing four groups of minerals in coal samples, including clay, carbonate, quartz and phosphates. These minerals have different properties in coal seams. As shown in Table 1, in SY1, the dominant mineral was clay (kaolinite) with minor quartz and carbonates (dolomite and aklimaite). Similarly, in SY2, the major mineral was kaolinite with minor quartz, and traces of siderite, aklimaite and hydroxylapatite. The mineral content of SY3 was different mainly composed of carbonates, including the dominant ankerite, traces of siderite, and minimal content of quartz. In general, kaolinite is a commonly occurring mineral in coal as epigenetic cleat infillings (Spears and Caswell 1986). Quartz is the most common oxide mineral occurring in coal and largely appears as discrete grains of detrital origin. Phosphates often coexist with clay minerals, mainly present in the form of cell and pore infillings. In addition, a wide range of carbonate minerals have been reported in coal with most found as siderite, calcite, dolomite and ankerite. Ankerite appears in cleat infillings and broken cell cavities within organic matters. It is noted that the volume of whole minerals in each experimental specimen was measured from  $\mu$ CT images.

### Triaxial $\mu$ CT imaging

The schematic view of the X-ray imaging triaxial system (Roshan et al. 2019a) is shown in Fig. 1. The system has independent controls for axial and confining stresses with fluid flow access to the specimen through the inner hole at

**Table 1** Mineral (crystalline) compounds from XRD analysis

Mineral Contents		Categories (%)		
Phases	Chemical Formula	SY1	SY2	SY3
Kaolinite	$\text{Al}_2\text{O}_3 \cdot 2\text{SiO}_2 \cdot 2\text{H}_2\text{O}$	76.6	69.5	
Quartz	$\text{SiO}_2$	3.5	4.3	1.3
Dolomite	$\text{MgCO}_3 \cdot \text{CaCO}_3$	13.5		
Aklimaite	$\text{Ca}_4(\text{Si}_2\text{O}_5(\text{OH})_2)(\text{OH})_4 \cdot 5(\text{H}_2\text{O})$	6.3	9.7	
Siderite	$\text{Mg}_{0.35}\text{Fe}_{0.65}(\text{CO}_3)$		9.2	0.8
Hydroxylapatite	$\text{Ca}_5(\text{PO}_4)_3(\text{OH})$		7.3	
Ankerite	$\text{Ca Mg}_{0.46}\text{Fe}_{0.54}(\text{CO}_3)_2$			97.9

both end platens. Similar to a traditional triaxial cell, the coal specimen was hosted in a rubber sleeve to isolate it from confining oil. The axial load was applied through a micro-ram which placed on the top platen of the triaxial cell. In the axial direction, the system has both displacement and load control, but only load control was used in this study. Three ISCO pumps were used to control axial, radial and fluid pressures and the pressure transducers were connected to the pressure lines. The fluid flow section allowed both drained and undrained testing conditions by opening or closing the downstream outlet at the bottom platen. The X-ray scanning used in the study is in helical mode, meaning that the triaxial cell rotates along its axis while the X-ray source and the detector maintain stationary. An X-ray source with a voltage of 100 kV and a current of 120  $\mu$ A were used for scanning. This setup yields an image resolution of 12.4  $\mu$ m with about 2-h scanning time on the specimen (Chen et al. 2020; Pirzada et al. 2021). To study the relation between mineral content and hydromechanical properties, images should be processed and segmented into three domains: mineral, organic matter and fracture. The image processing will be discussed later. To measure the bulk compressibility,  $C_{bc}$  for example, we scanned the specimen twice under different confining pressures, and then measured the volume difference of the two obtained images. The fracture porosity reported in the plots is those at the second stage of testing (specimen compressed).

Table 2 summarizes the stress-pressure conditions of XRCT imaging to obtain the hydromechanical properties (compressibility of system components including bulk,

**Table 2** Image-driven hydromechanical tests and parameters

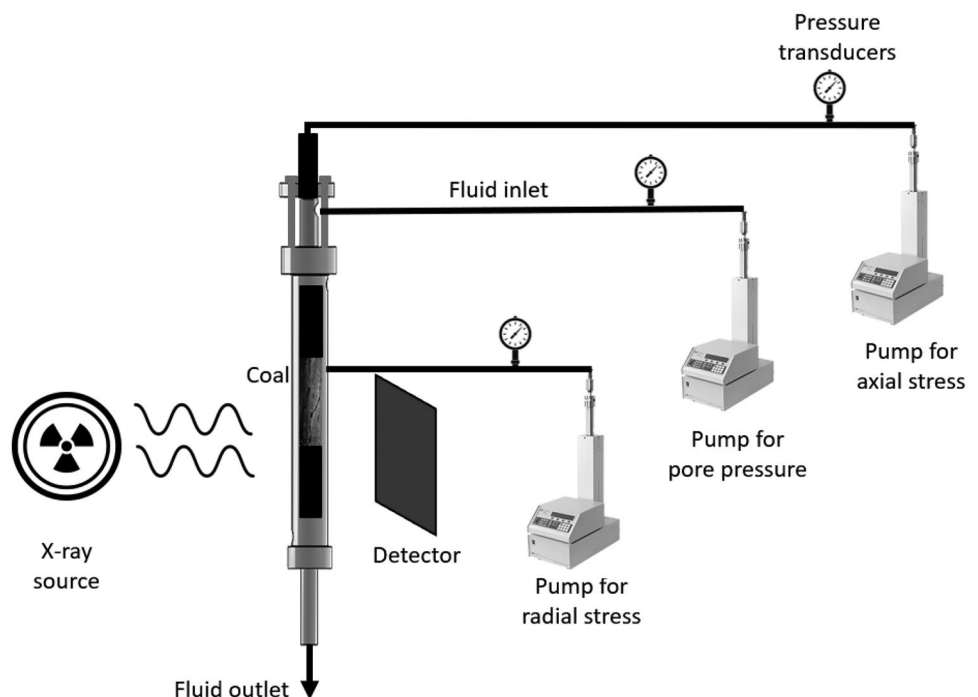
Type of test	Testing condition		Measured hydromechanical parameters
	Constant	Variable	
Unjacketed BC	$P_d$	$\sigma, p$	$C_s$
Drained BC-1	$\sigma$	$p$	$C_{fp}, C_{bp}$
Drained BC-2	$p$	$\sigma$	$C_{fc}, C_{bc}, \gamma$
Adsorption BC	$p$ and $\sigma$	Gas type	-

fracture and solid constitutes). We conducted three groups of tests to determine the system compressibilities and find their relationships with samples' mineral content and fractures including Unjacketed BC, Drained BC1 and Drained BC2. In unjacketed test,  $C_s$  was determined by maintaining a constant  $P_d$  as in Eq. (5). The first drained test was conducted at a constant p and the second drained test was performed at a constant  $\sigma$ . The bulk and fracture compressibilities were studied in two drained tests with different boundary conditions (Eqs. 3 and 4). An extra set of tests were carried out with both sorbing and non-sorbing gases to investigate the swelling effect on hydromechanical properties.

**Unjacketed BC**

The original unjacketed test (Biot and Willis 1957) involves immersing the sample in pressurised fluid, so the fluid can penetrate through pores of the sample. This method was later modified to an unjacketed test using a triaxial cell under

**Fig. 1** A schematic view of X-ray transparent triaxial system





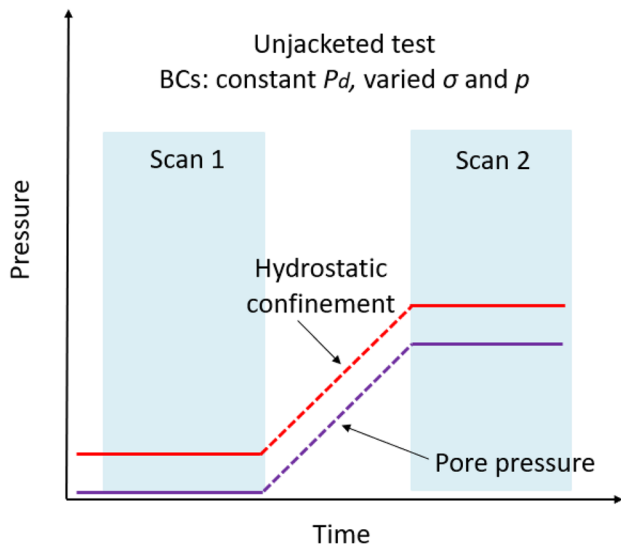


**Fig. 2** Test design in Unjacketed BC using two scans to measure the solid compressibility at constant differential pressure

undrained conditions. As shown in Fig. 2, a constant differential pressure  $P_d$  is maintained throughout the test, with both  $\sigma$  and  $p$  increasing by the same amount and stay close to each other. To use this method in XRCT imaging experiment, two scans were performed (see Fig. 2). By measuring the applied volumetric strain from both images, the solid compressibility,  $C_s$  can be calculated using Eq. (5) which is the gradient of volumetric strain to stress. Three specimens (SY1, SY2 and SY3-1) were used for these experiments under identical BCs, as shown in Table 3. The three specimens had a range of different mineral contents (~2%-26%) and type of minerals (clay-rich versus calcite-rich). Different mineral types were chosen for the analysis to capture their effect on overall solid compressibility of the system. It is also noted that the fracture porosity of the specimens is not central in analysis of solid compressibility.

**Drained BC-1**

This group of tests aims to acquire the bulk and fracture compressibilities,  $C_{bp}$  and  $C_{fp}$  using the boundary condition

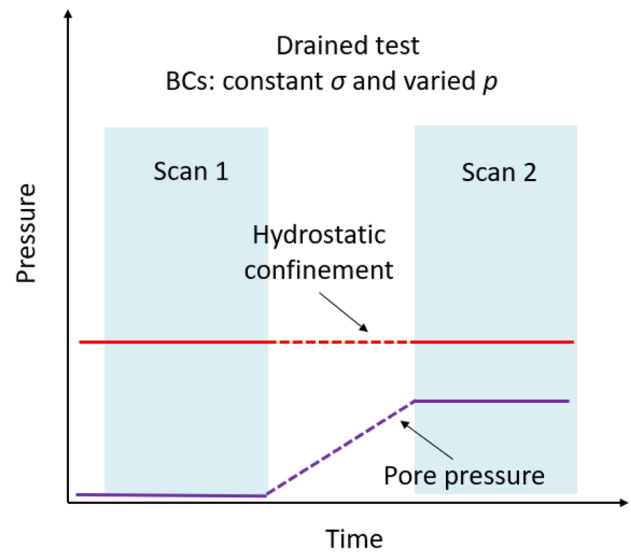


**Fig. 3** Test design in Drained BC-1 using two scans to measure the bulk and fracture compressibility at constant hydrostatics pressure

specified in Table 2. In these experiments,  $p$  was increased, while  $\sigma$  was maintained constant, so the volume change of bulk and fractures due to pore pressure increase could be characterized. Figure 3 shows the test procedure including the scanning sequence. It is noted the hydrostatic confinement was kept constant but different in each test while the pore pressure was increased. Three specimens were tested in this group as shown in Table 4. All specimens were from category SY3 (SY3-1, SY3-3, and SY3-4) having different mineral contents (~25%-35%) and fracture porosity (~0.3%-0.8%) but the same mineral constituents (calcite-rich). As the fracture compressibility is of particular importance in this test, a range of specimens with high fracture porosity variation was chosen.

**Drained BC-2**

In the Drained BC-2, the gas was allowed to flow out of the sample during external loading ( $\sigma$ ) while keeping the pore pressure,  $p$  constant. The change of the bulk and fracture volumes were then measured. As the fluid pressure

**Table 3** Test design and specimens used in the Unjacketed BC

Specimen	Scan sequence	Gas type	Uniform stress	Pore pressure	Differential pressure
SY1	1	Helium	0.5 MPa	0	0.5 MPa
	2		3 MPa	2.5 MPa	
SY2	1		0.5 MPa	0	
	2		3 MPa	2.5 MPa	
SY3-1	1		0.5 MPa	0	
	2		3 MPa	2.5 MPa	

**Table 4** Test design and specimens used in the Drained BC-1

Specimen	Scan sequence	Gas type	Uniform stress	Pore pressure
SY3-1	1	Helium	3 MPa	0
	2			2.5
SY3-3	1		4 MPa	0
	2			3.5
SY3-4	1		5 MPa	0
	2			4.5

throughout the loading is identical,  $\Delta V_f$  represents the change of fracture volume resulted from the incremental loading. From this group of tests, the drained bulk compressibility ( $C_{bc}$ ), the fracture compressibility ( $C_{fc}$ ) and ESC ( $\gamma$ ) can be determined. Figure 4 shows the loading path and the sequence of two scans at this BC. The outlet line was opened to atmospheric pressure thus the pore pressure was maintained constant. Hydrostatic confinement was increased from the first scan to the second, to compress the specimen. Comparing the volume difference in the bulk and fractures from the two scans,  $C_{bc}$  and  $C_{fc}$  can be calculated. Two specimens (SY3-1 and SY3-4) were used in the experimental design of this group, as shown in Table 5. These two specimens have similar mineral-type (calcite-rich), fracture porosity (0.66% and 0.62%, respectively) and mineral content (25.4% and 29.3%, respectively) but different mineral structures (isolated versus spread) chosen with the view of investigating mineral structure.

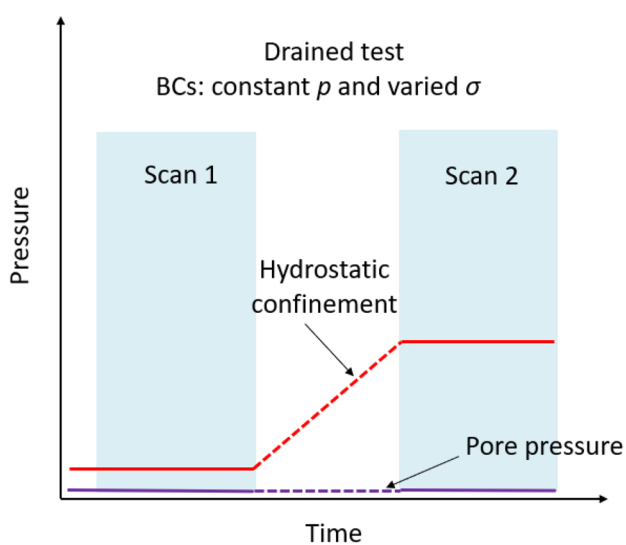


**Fig. 4** Test condition in Drained BC-2 using two scans to measure the bulk and fracture compressibility at the constant pore pressure

**Table 5** Test design and specimens used in the Drained BC-2

Specimen	Scan sequence	Uniform stress
SY3-1	1	0.5 MPa
	2	3 MPa
SY3-4	1	0.5 MPa
	2	3 MPa

**Adsorption BC (sorption-hydromechanical effect)**

An additional group of tests was carried out on three specimens (SY2, SY3-2 and SY3-3) with sorbing gas to investigate the effect of swelling on hydromechanical response. It is noted that these three specimens had different fracture porosity (~0.3%-0.8%), different mineral contents (~2.5%-32%) and different minerals type (clay-rich and calcite-rich) thus a combination of different factors on swelling behaviour was considered. It is well known that carbon has an adsorptive nature and coal shows swelling when exposed to sorbing gas. The specimens were first saturated by helium and then by CO<sub>2</sub> and they were scanned in turns at the BCs shown in Fig. 5. As the gas adsorption amount is dependent on the pore pressure, a consistent pore pressure of 2.5 MPa was applied to eliminate the pressure effects. Time (1–2 days) was given to CO<sub>2</sub> to saturate the specimen and reached an adsorption equilibrium. Three specimens used in this group and their experimental BCs are presented in Table 6.

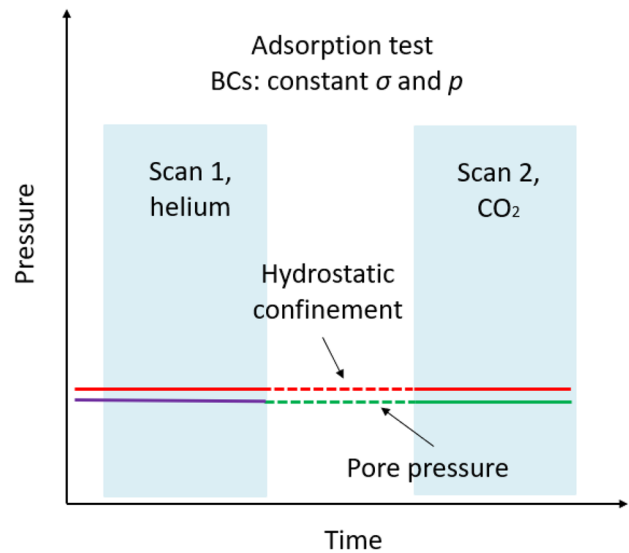


**Fig. 5** Test condition in adsorption BC using two scans to measure the effect of adsorption on hydromechanical response

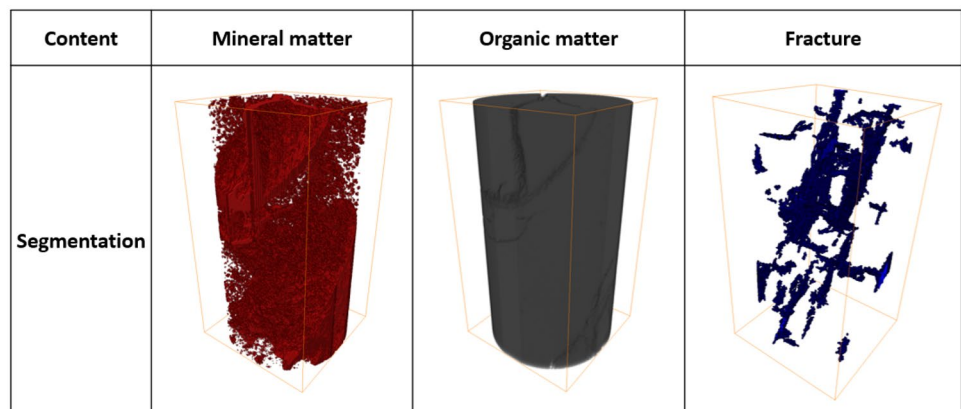
**Table 6** Test design and specimens in adsorption test using helium and CO<sub>2</sub>

Specimen	Scan sequence	Gas type	Pore pressure
SY2	1	Helium	2.5 MPa
	2	CO <sub>2</sub>	
SY3-2	3	Helium	
	4	CO <sub>2</sub>	
SY3-3	5	Helium	
	6	CO <sub>2</sub>	

## Image processing

After performing experiments, the obtained 3D XRCT images were processed and analysed. In this study, the commercial software AVIZO (FEI Group 2013) was used for volume editing, registration, denoising, segmentation, etc. As a first step, the images were denoised using multiple filter, e.g. the non-local means filter was used to replace the grey value of a pixel with an average of the grey values of nearby pixels (Buades et al. 2005; Matsuoka et al. 2017). The images from each set of experiment were then aligned geometrically for registration purpose which can additionally enable investigating variation in the volume of each component. Images were next segmented into three domains of mineral, organic matter and fracture. Segmentation was performed by combined methods of grayscale thresholding, watershed algorithm and magic wand tool (Thermo-Fisher-Scientific 2018). Grayscale thresholding is a simple approach to segment different domains using grayscale values. Watershed is an interactive thresholding which provides a statistical algorithm to assign each pixel to a region or a watershed (Beucher and Meyer 2018; Preim and Botha 2013). Magic wand tool is a quick method to segment irregularly shaped regions based on edges. Suitable application of combined processing methods yields an ideal segmentation. Figure 6 shows typical segmented domains of a coal specimen from a 3D image.

**Fig. 6** Segmentation of mineral, organic matter, and fracture domains of a 3D image



## Bulk deformation calculation

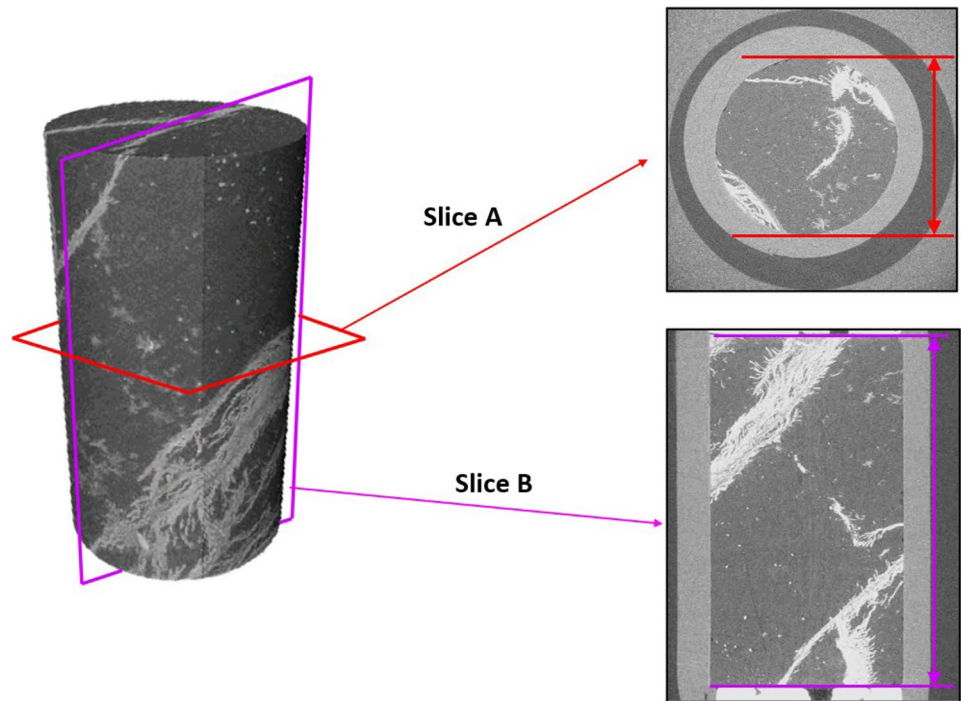
To measure the specimen deformation at different BCs, the diameter and length of specimen at the corresponding reconstructed 3D images were measured, as shown schematically in Fig. 7. A pair of tomography images from orthogonal planes were extracted from the 3D image, while the specimen diameter and height were measured from the horizontal (slice A in Fig. 7) and vertical (slice B in Fig. 7) cross sections, respectively. Multiple measurements were performed, and the average value was considered in the analysis. The accuracy of the measurement sits within the obtained image resolution of 12.4  $\mu\text{m}$ .

## Validation study

To assess the validity of measured hydromechanical properties from XRCT images, the bulk and solid compressibilities, as well as ESC of the specimens' category SY3, were measured using conventional triaxial experiments. It is noted that this validation exercise with one specimen is to ensure that the measurements and calculation are of high quality as the accuracy of image-extracted properties including deformation has been already proven (Pone et al. 2010; Salemi et al. 2021; Sufian and Russell 2013; Viggiani and Hall 2008). To do so, we modified the previously in-house designed triaxial cell (Roshan et al. 2019b) to adapt the specimen with a diameter of 0.5 inch ( $\sim 12.5$  mm) as shown in Fig. 8. The axial load on the sample was applied through a servo-controlled loading frame with capacity of 500 kN. Axial deformation was measured through the LVDT along the axial direction. Radial deformation was measured using the internal LVDTs. These deformations were logged using a LabView interface and recorded in the computer. A manual pump with hydraulic oil was used for confining pressure and gas cylinder with a regulator for the fluid pressure.



**Fig. 7** Measurement of the bulk deformation in reconstructed 3D images; Slice **A** for diameter measurement and slice **B** for length measurement



To obtain the ESC using the triaxial system, we measured bulk modulus in a drained experiment and solid bulk modulus in an unjacketed experiment, as summarised in Table 7 and detailed in Fig. 9. It is noted that the bulk modulus is inverse of bulk compressibility. In the drained experiment, the confining pressure was increased by  $\Delta\sigma$ , while the pore pressure  $p$  was maintained constant. The confining pressure

was increased by applying a loading rate of 0.18 mm/min, and the volumetric strain was continuously measured. The derivative of  $\sigma$  with respect to  $V_b$  is the bulk modulus,  $K_b$ . The solid modulus,  $K_s$  was measured in a jacketed experiment, with a boundary condition of constant differential pressure,  $P_d$  as previously discussed. As shown in Fig. 9, after each pressure increase ( $\Delta p$ ), the difference between

**Fig. 8** Triaxial system for hydromechanical experiments

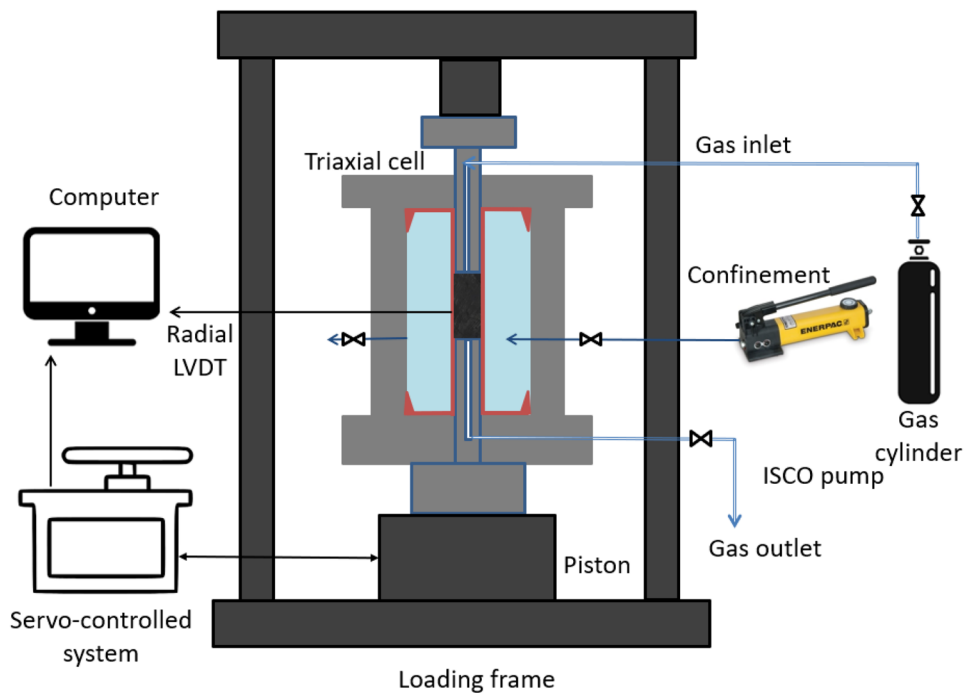


**Table 7** Experimental measurements to obtain ESC by performing the triaxial experiments

Specimen	Property calculated	Property measured	Triaxial experiment
SY3-4	ESC	Bulk modulus/bulk compressibility Solid modulus/solid compressibility	Drained experiment Unjacketed experiment

the confining pressure and pore pressure was maintained unchanged (close to each other) which allowed the volumetric strain reaching equilibrium, enabling the measurement of  $\Delta V_b$ . The pressure was plotted versus volumetric strain obtained at each step, and then, the effective stress coefficient was determined following Eqs. ((3), (5)–(7)).

**Comparison of measurements using triaxial cell and XRCT imaging**

As noted above, the bulk modulus was measured through a uniform loading where the  $K$  is the gradient of stress to volumetric strain. The solid bulk modulus was measured in

a stepwise test, where a constant differential pressure was applied to calculate  $K_s$ . These two gradients measured from both measurements are presented in Fig. 10. The mechanical tests yielded a bulk modulus of 1.019 GPa and a solid bulk modulus of 8.8 GPa. Therefore, the effective stress coefficient was calculated to be 0.88.

The same set of above parameters were calculated from XRCT images. As shown in Fig. 11, the first image was taken without stress and the second under 5 MPa uniform stress. Comparing 2D tomograph from two images, as highlighted in red circle on images, the fracture porosity and fracture size in the first image are higher than that of the second image. From the raw image slices shown, the fracture

**Fig. 9** Measurements of  $K$  and  $K_s$  from triaxial experiment

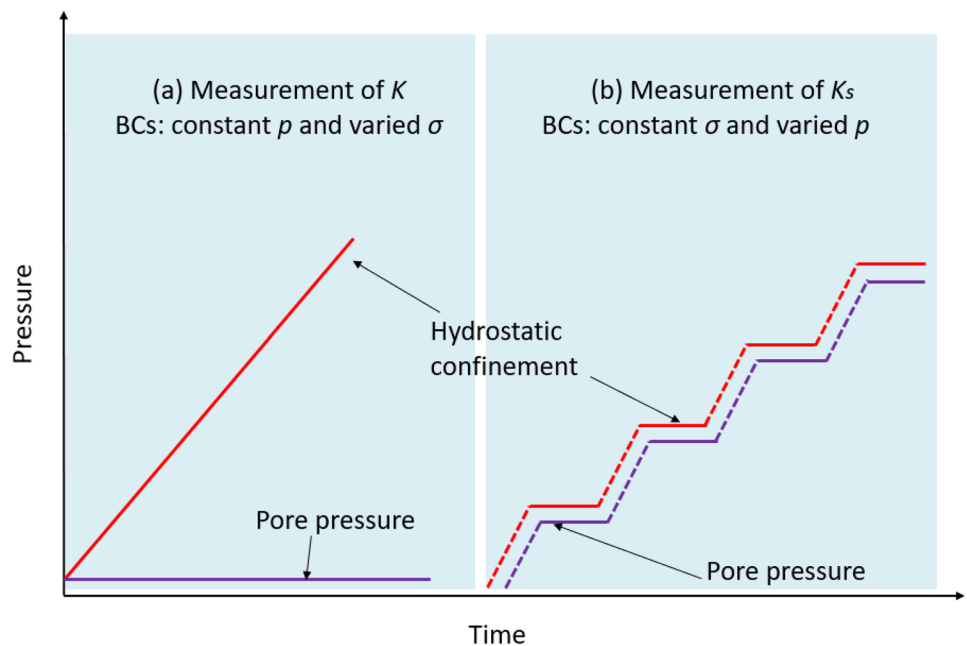
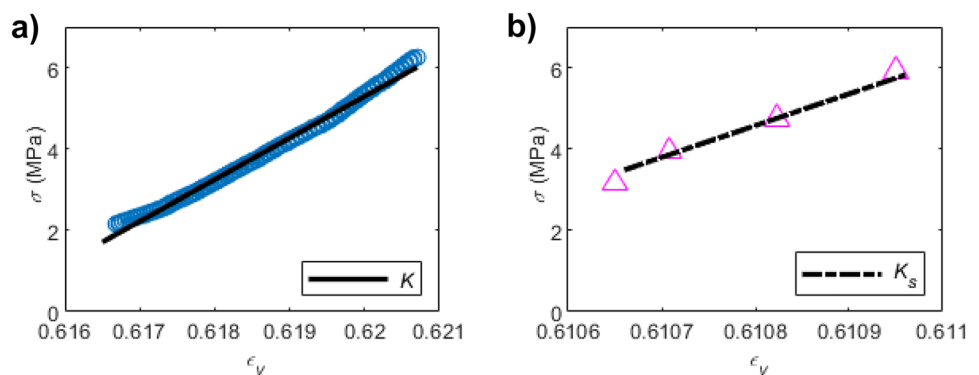


**Fig. 10** Hydromechanical testing of bulk modulus and solid bulk modulus; **a** uniform compression test yields bulk modulus of 1.019 GPa and **b** solid bulk modulus of 8.8 GPa



aperture reduces from around 50 microns to less than 13 microns, and the number of fractures reduces from more than 10 to only 2 small discrete fractures. After segmentation, the fracture domain was extracted from two images showing an evident closure of fractures induced by stress. Having the fracture and bulk volumetric strains, the effective stress coefficient is calculated as 0.89 using Eq. 8. Similarly, bulk modulus can be calculated using Eq. 3 through the uniform compression and solid bulk modulus can be inferred from Eq. 7. Results from both approaches are presented in Table 8 showing a high level of confidence in the methodology adopted.

## Results and discussion

### Hydromechanical response

#### Unjacketed BC (constant differential pressure)

In the unjacketed testing group, two scans were taken under the same differential pressure for specimens SY1, SY2 and SY3-1 having different mineralogy and minerals content. Figure 12 illustrates the stress and helium pore pressure

**Table 8** Bulk modulus, solid bulk modulus and Biot’s coefficient measured from two approaches

	Bulk modulus (GPa)	Solid bulk modulus (GPa)	Effective stress coefficient
Experiment	1.0	8.8	0.88
XRCT image	1.1	10.1	0.89

conditions of the tests plus their tomography images for each specimen, i.e. the first scan was taken at 0.5 MPa stress with no pore pressure, and the second scan was taken at a total stress of 3 MPa with helium pressure of 2.5 MPa for all specimens. To precisely calculate the fracture volume and investigate the relation between the sample compressibility and mineral content, images were segmented into three domains: fracture, mineral and organic matter (Fig. 13).

As specimens were cored from different samples, they showed distinct mineral compositions and structure. Figure 12 shows that SY1 and SY2 have relatively low amount of mineral (8.7% and 2.5% volume ratio, respectively, from XRCT analysis) with kaolinite clay being the dominant mineral from XRD analysis (Table 1). Minerals in SY1 have a lamellar structure, while SY2 has scattered and dotlike minerals

**Fig. 11.** 2D tomograph images and segmented fractures of specimen SY3-4 (atmospheric pore pressure)

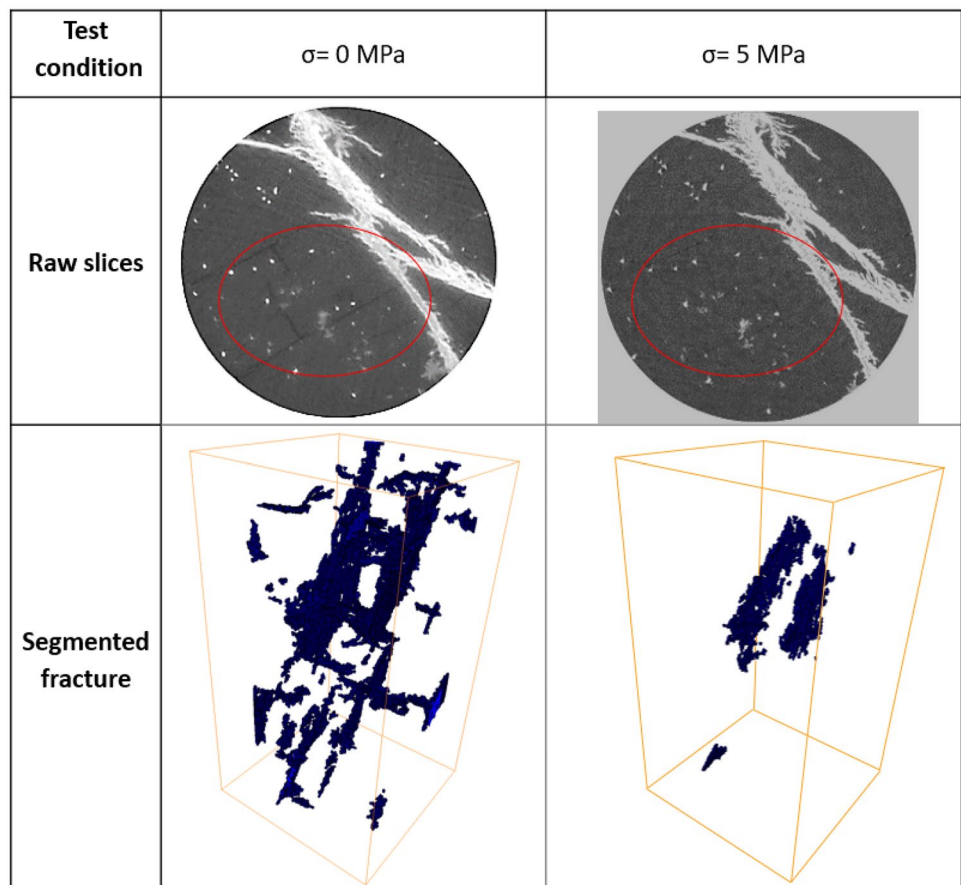
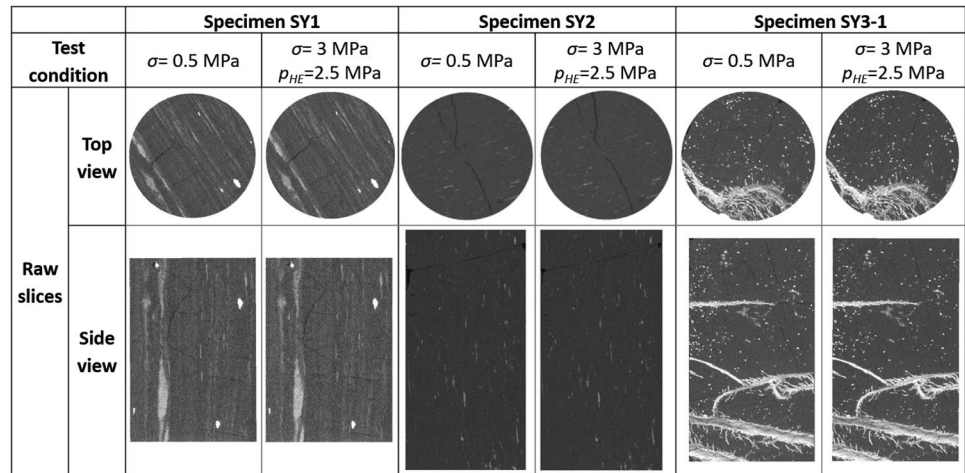


**Fig. 12** Tomograph images from three specimens of different mineral contents tested with helium in unjacketed BC



distribution. From the tomography images (see Fig. 12), kaolinite appears to be well ordered and in bands and laminae due to its in situ leaching and reprecipitation within the peat swamp (Ward 1989). SY3-1, however, contains large amounts of carbonates with authigenic structure (25.2% volume ratio from XRCT analysis (see Fig. 13)). They were formed during deposition and coalification process (Taylor et al. 1998; Ward 1992) and seem to be infillings of fractures as well as veining in the matrix structure. This has a high potential to stiffen the bulk of coal and reduces its compressibility.

From these experiments, the solid compressibility,  $C_s$ , or its inverse, the solid bulk modulus,  $K_s$ , of different categories were measured and presented in Fig. 14 as a function of mineral content. Interestingly, the  $K_s$  shows a positive nonlinear trend with an increase in the mineral content irrespective of the mineral type. It emphasizes that organic matter compressibility is higher than other minerals whether it is composed of soft (clay) or hard (carbonate) minerals. Different from those of SY1 and SY2, minerals in SY3-1 are majority carbonate with high stiffness and low compressibility compared to clay minerals in other samples. Despite the higher stiffness of calcite compared to clay minerals and that SY3-1 contains much higher minerals than SY1 and SY2 (25.2%, 2.5% and 8.7% for SY3-1, SY2 and SY1, respectively), the rate of increase in compressibility with mineral content reduces at higher mineral volumes. It has been inferred that ions in the carbonates originated from organic matters during coal rank advancement mainly fill in the coalbed fractures through fluid migration (Spears and Caswell 1986).

#### Drained BC-1 (constant hydrostatic stress)

Tomograph slices along with 3D segmented images from Drain BC-1 for three specimens of the same category SY3 (SY3-1, SY3-3 and SY3-4) are shown in Fig. 15, where different pore pressures of helium at a constant hydrostatic pressure were applied on each specimen. It is noted that the

pore pressure and stresses were different for each specimen but the condition of constant confining (hydrostatic) stress at varying pore pressures was maintained. All the specimens were prepared from the same sample to present a similar type of mineral (calcite-rich). Figure 15 shows that SY3-3 has the highest mineral content (34.21% volume ratio) compared to others (25.2% and 29.3% volume ratio for SY3-1 and SY3-4, respectively). An increase in the pore pressure leads to opening of fractures in all specimens but to a different extent. Interestingly, the fracture opening by fluid pressure follows the mineral content; higher the mineral content, the less fracture opening by increase in pore pressure. The fracture opening in SY3-1 was the highest, followed by SY3-4 and SY3-3. A gradual decrease was observed in both  $C_{fp}$  and  $C_{bp}$  with an increase in the mineral content, while an increasing trend was observed with fracture porosity (Fig. 16). Similar positive correlation between  $C_{fp}$  and fracture porosity has also been reported by Zhu et al. (2018) and Bagherzadeh et al. (2021). The results, however, suggest that fracture compressibility is much more sensitive to increase in pore pressure than the bulk compressibility. This behaviour also emphasises that the effect of minerals on the hydromechanical behaviour of fracture and bulk is different. In fact, the findings of this study evidently show that an increase in mineral content stiffens the coal skeleton more efficiently than the absence of fracture.

#### Drained BC-2 (constant pore pressure)

Similar to the Drained BC-1, both fracture and matrix compressibilities,  $C_{fc}$  and  $C_{bc}$  were measured but at a constant pore pressure (atmospheric) with varying hydrostatic stress (see Figs. 17 and 18). The ESC was also calculated in this analysis. Both specimens used in this analysis, were highly cleated with high fracture porosity (0.66% and 0.62%) and a minor difference in mineral content (volume ratio of 25.4% and 29.3% for SY3-1 and SY3-4, respectively, Fig. 17). The



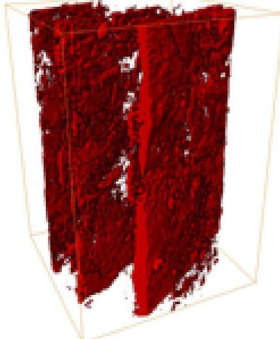
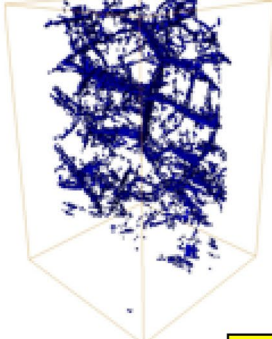
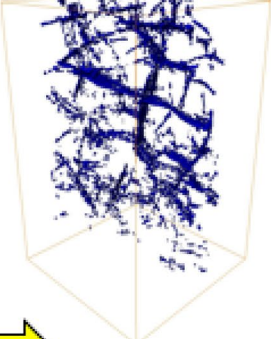
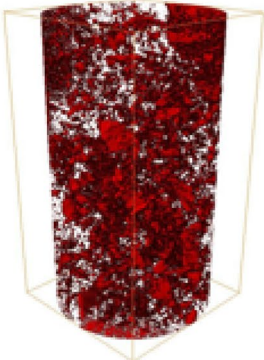
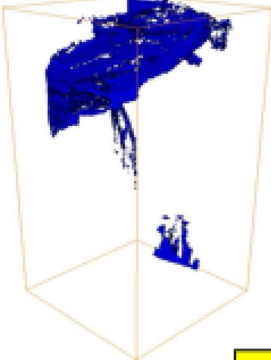
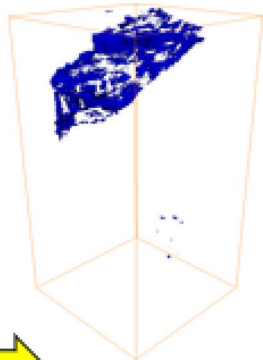
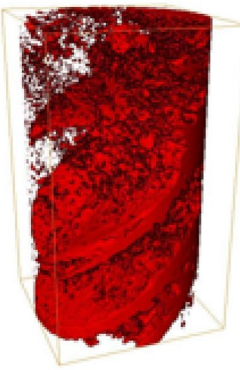
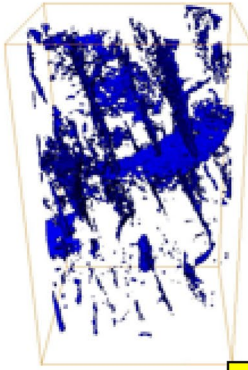
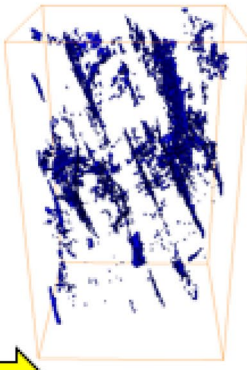
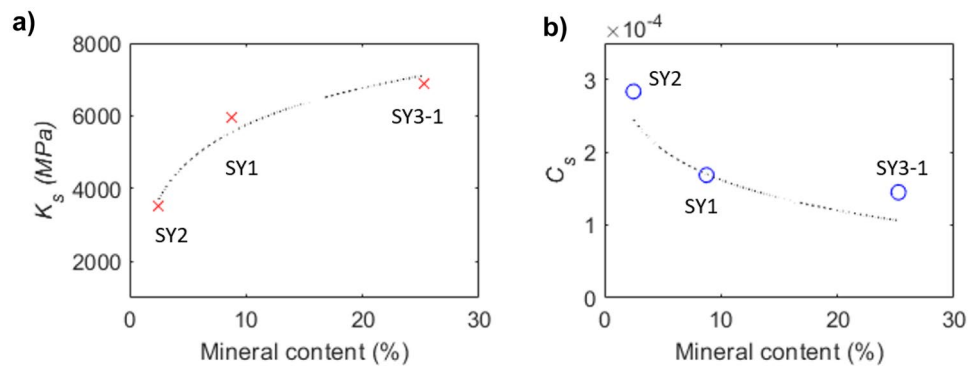
	Mineral domain	Fracture domain	
Test condition	$\sigma = 0.5 \text{ MPa}$	$\sigma = 0.5 \text{ MPa}$	$\sigma = 3 \text{ MPa}$ $p_{HE} = 2.5 \text{ MPa}$
Specimen SY1			
	Mineral content=8.76%	Fracture volume reduced by 37.2%	
Specimen SY2			
	Mineral content=2.49%	Fracture volume reduced by 44.7%	
Specimen SY3-1			
	Mineral content=25.24%	Fracture volume reduced by 27.6%	

Fig. 13 Mineral and fracture domains of specimen SY1, SY2 and SY3-1 in unjacketed BC



**Fig. 14.** **a**  $K_s$  as a function of mineral content (volume ratio) and **b**  $C_s$  as a function of mineral content (volume ratio) in unjacketed BC.



increase in hydrostatic stress resulted in a decrease in the fracture porosity of both specimens, but at different rates. In SY3-1, the volume of fractures was uniformly reduced while in SY3-4, two main fractures were remained partially open after compression. This difference resulted in a greater value of bulk compressibility in SY3-1. The fracture compressibility of both specimens was, on the other hand, considerably different. The non-uniform fracture closure in SY3-4 was controlled by the structure of minerals. While fractures in SY3-1 were more evenly distributed in the bulk of the specimen, in SY3-4, fractures were preferably aligned and relatively isolated. Thus, the reduction of volume due to compression in SY3-4 was localised. The ESC was also found to be dependent to both the fracture porosity

and mineral content. The higher fracture porosity and lower mineral content leads to a higher ESC (Fig. 18). This is intuitive as the increase in the mineral content and reduction of fracture porosity will lead to an increase in the load bearing capacity of the skeleton and consequently reduction of the bulk compressibility.

**Adsorption (sorption-hydromechanical effect)**

To investigate the combined effect of minerals and fractures on bulk and matrix deformation in presence of a sorbing gas, a set of experiments were conducted on specimens SY2 and SY3-2 and SY3-3 (Table 9). It is important to note that the mineral content of specimen SY2 (2.5%

	Specimen SY3-1		Specimen SY3-3		Specimen SY3-4	
Mineral content	25.2%		34.2%		29.3%	
Confining pressure	$\sigma=3$ MPa		$\sigma=4$ MPa		$\sigma=5$ MPa	
Gas pressure	$p_{HE}=0$	$p_{HE}=2.5$ MPa	$p_{HE}=0$	$p_{HE}=3.5$ MPa	$p_{HE}=0$	$p_{HE}=4.5$ MPa
Raw slices						
Segmented fractures						

**Fig. 15** Fracture domain in three specimens used in Drained BC-1

**Fig. 16** Results in Drained BC-1; a1)  $C_{bp}$  as a function of mineral content, a2)  $C_{bp}$  as a function of fracture porosity, b1)  $C_{fp}$  as a function of mineral content and b2)  $C_{fp}$  as a function of fracture porosity

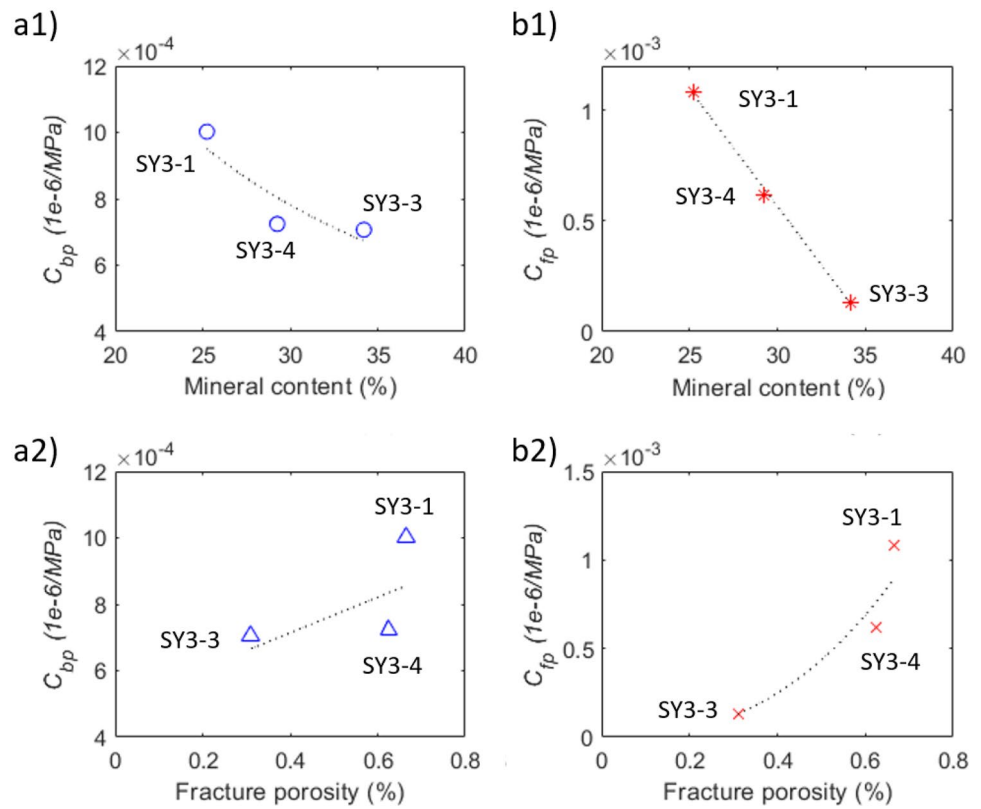


**Fig. 17** Tomograph images and segmented fractures of two specimens used in Drained BC-2

	Specimen SY3-1		Specimen SY3-4	
Mineral content	25.2%		29.3%	
Test condition	$\sigma = 0.5$ MPa	$\sigma = 3$ MPa	$\sigma = 0.5$ MPa	$\sigma = 3$ MPa
Raw slices				
Segmented fracture				

volume ratio) was considerably lower than the two specimens from category SY-3 (31.5% and 34.2% volume ratios for SY3-2 and SY3-3, respectively). The gas pore pressure of 2.5 MPa was first applied on each specimen, using a non-sorbing gas (helium), followed by injection of sorbed gas (CO<sub>2</sub>) at constant hydrostatic pressure of 3 MPa. The 2D tomograph images and segmented fractures are illustrated in Fig. 19 showing that the SY3-3 specimen contains the highest number of fractures while the others contain a single main fracture through the bulk of the

**Table 9** Matrix swelling strain and volume content of system components in three specimens used for adsorption test

Specimen number	Matrix swelling strain (%)	Volume Content		
		Mineral content (%)	Organic matter content (%)	Fracture porosity (~ %)
#SY2	2.9	2.5	96.8	0.69
#SY3-2	2.1	31.5	48.8	0.80
#SY3-3	1.6	34.2	65.5	0.30

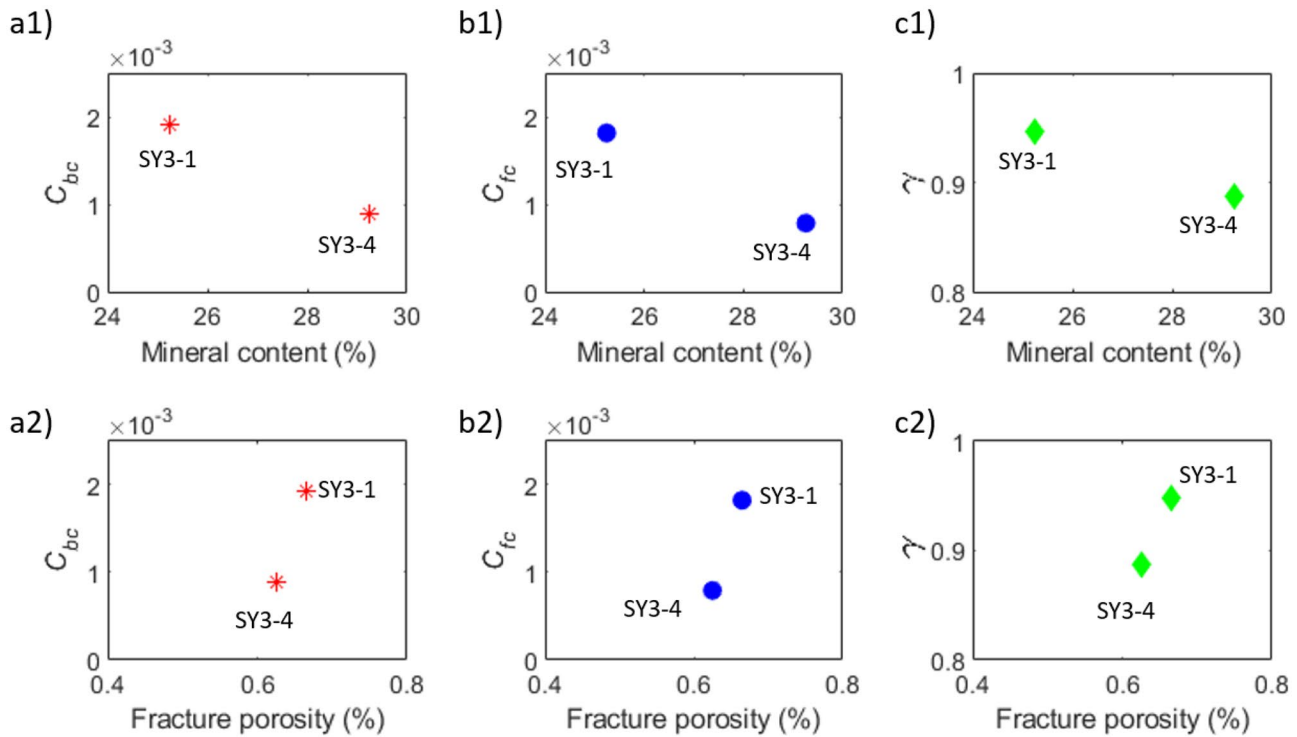


**Fig. 18** Results in Drained BC-2; a1)  $C_{bc}$  as a function of mineral content, a2)  $C_{bc}$  as a function of fracture porosity, b1)  $C_{fc}$  as a function of mineral content, b2)  $C_{fc}$  as a function of fracture porosity, c1)

effective stress coefficient as a function of mineral content, and c2) effective stress coefficient as a function of fracture porosity

specimens (the specimens have fracture porosity ranging from ~0.3%-0.8%).

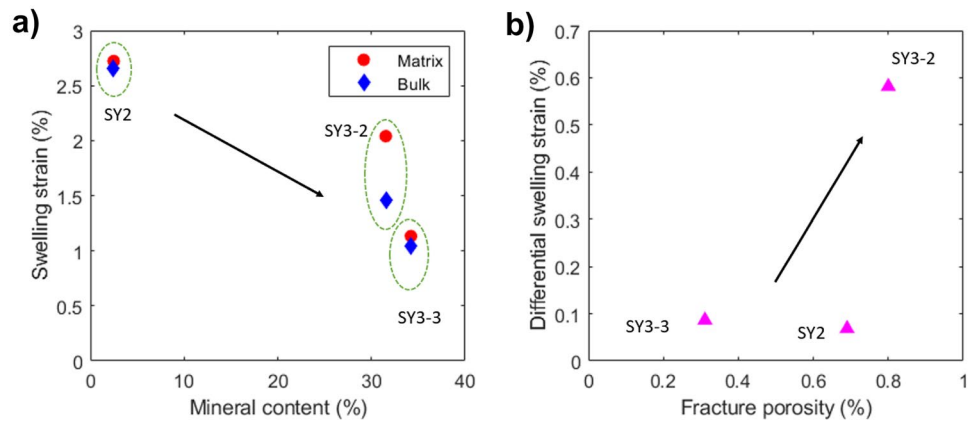
The sorbing gases cause the coal to swell, resulting in an increase in the matrix and bulk volumetric strain and a reduction in internal fracture volume. By calculating solid volume excluding fractures, we obtained the bulk and matrix deformation between the treatment of helium and CO<sub>2</sub> and plotted it versus mineral content in Fig. 20. It can

be observed from this figure that SY2 has the largest swelling strain both in bulk and matrix as it contains a negligible amount of mineral (2.5% volume ratio) and high content of organic matter (96.8% volume ratio) with a single fracture (with high porosity due to its fracture aperture). Specimens from SY3 category showed lower matrix-bulk swelling. This is attributed to presence of high volume of carbonate minerals that reduces the micropore volume (Mastalerz

**Fig. 19.** 2D tomograph images and segmented fractures for three specimens, saturated by helium and CO<sub>2</sub>

	Specimen SY2		Specimen SY3-2		Specimen SY3-3	
Mineral content	2.5%		31.5%		34.2%	
Gas pressure	$p_{He}=2.5$ MPa	$p_{CO_2}=2.5$ MPa	$p_{He}=2.5$ MPa	$p_{CO_2}=2.5$ MPa	$p_{He}=2.5$ MPa	$p_{CO_2}=2.5$ MPa
Raw slices						
Segmented fractures						

**Fig. 20** Effect of mineral content and fracture porosity on swelling strain of three specimens; **a)** matrix and bulk swelling as a function of mineral content, and **b)** differential swelling strain between matrix and bulk as a function of fracture porosity



et al. 2008) thus has negative impact on adsorption effect. This is in agreement with the findings of previous studies (Zhang et al. 2020).

It is interesting to note that the greatest difference in swelling strain between the bulk and matrix was found in SY3-2, while minimal differences were observed in other specimens. The aperture (opening) of fractures in SY3-2 was much greater than those of other specimens (highest fracture porosity). It implies that specimens with widely open fractures show less bulk swelling as fractures tend to absorb the coal matrix swelling internally thus leading to less bulk swelling when under external stress. Overall, the volumetric strain is highly influenced by both mineral content and fracture structure in the adsorption process.

## Conclusions

In this study, the effect of mineral content and structure together with their combined effect of fracture porosity on the hydromechanical response of fractured coal specimens was experimentally evaluated. With the combined method of XRCT visualization and triaxial testing, we performed unjacketed and drained tests and calculated the effective stress and a range of system compressibilities through image processing. This image-based calculations were validated with a standard triaxial experiment. The results of this study show that the solid bulk modulus of coal  $K_s$  has a positive nonlinear relationship with mineral content irrespective of the mineral type. In general, the coal fracture compressibility is negatively correlated to the mineral content, while the matrix compressibility is positively correlated to the fracture porosity. Specially, carbonates as infillings strengthen the coal matrix. Specimens in this study show that kaolinite are well ordered and appears in bands and laminae while carbonate appears in authigenic

pattern. As a result, specimens with low content of minerals containing dominant kaolinite are more compressible than those containing high content of carbonate. It was also found that the fracture opening by internal fluid pressure follows the mineral content; the higher mineral content, the less fracture opening due to increase in pore pressure. Also, the results suggest that the change in fracture compressibility is much more sensitive to pore pressure increase than bulk compressibility. Interestingly, the results further indicate that the minerals can considerably stiffen the skeleton much more efficiently than the absence of fracture in the coal specimens. The effective stress coefficient is also found to be a complex function of not only the fracture porosity but also the mineral content. The higher fracture porosity and lower mineral content leads to a higher ESC. Finally, coal samples with more open fractures in the presence of adsorbing gas show less bulk swelling despite the higher swelling potential of their matrix. This shows that specimens with widely open fractures experience less bulk swelling as fractures tend to absorb the coal matrix swelling internally thus leading to less bulk swelling when under external stress. The findings of this study have significant implications in field studies such as gas production and injection in coal seams where the hydromechanical response of coal is important.

**Supplementary Information** The online version contains supplementary material available at <https://doi.org/10.1007/s10064-022-02669-0>.

**Acknowledgements** This work was supported by the Australian Coal Association Research Program (ACARP), project number C27027. Adelina Lv acknowledges the Australian Government Research Training Program for her scholarship. The authors acknowledge the UNSW Network Labs funded by the UNSW Research Infrastructure Scheme. They are Tyree X-ray CT Facility for the acquisition of the 3D XRCT images, and Mark Wainwright Analytical Center for the XRD analysis.

**Funding** Open Access funding enabled and organized by CAUL and its Member Institutions.



## Declarations

**Competing Interests** Authors declare that there is no conflict of interest.

**Open Access** This article is licensed under a Creative Commons Attribution 4.0 International License, which permits use, sharing, adaptation, distribution and reproduction in any medium or format, as long as you give appropriate credit to the original author(s) and the source, provide a link to the Creative Commons licence, and indicate if changes were made. The images or other third party material in this article are included in the article's Creative Commons licence, unless indicated otherwise in a credit line to the material. If material is not included in the article's Creative Commons licence and your intended use is not permitted by statutory regulation or exceeds the permitted use, you will need to obtain permission directly from the copyright holder. To view a copy of this licence, visit <http://creativecommons.org/licenses/by/4.0/>.

## References

- Ahamed M, Perera M, Matthai S, Ranjith P, Li D-Y (2019) Coal composition and structural variation with rank and its influence on the coal-moisture interactions under coal seam temperature conditions—A review article. *J Petrol Sci Eng* 180:901–917. <https://doi.org/10.1016/j.petrol.2019.06.007>
- Bachu S (2003) Screening and ranking of sedimentary basins for sequestration of CO<sub>2</sub> in geological media in response to climate change. *J Environ Geol* 44(3):277–289. [https://doi.org/10.1016/S0196-8904\(03\)00101-8](https://doi.org/10.1016/S0196-8904(03)00101-8)
- Bagherzadeh P, Goshtasbi K, Kazemzadeh E, Kashef M, Bakhtiari HA (2021) Stress-dependence of the permeability, porosity, and compressibility in fractured porous media regarding fracturing condition. *Bull Eng Geol Env* 80(6):5091–5110. <https://doi.org/10.1007/s10064-021-02215-4>
- Barbour T, Ko H-Y (1979) Relationship of mechanical, index, and mineralogic properties of coal measure rock. In the 20th US Symposium on Rock Mechanics (USRMS), Austin, Texas, USA
- Bertrand F, Buzzi O, Collin F (2019) Cleat-scale modelling of the coal permeability evolution due to sorption-induced strain. *Int J Coal Geol* 216:103320. <https://doi.org/10.1016/j.coal.2019.103320>
- Beucher S, Meyer F (2018) The morphological approach to segmentation: the watershed transformation. *Mathematical morphology in image processing*, Edn. 1st. CRC Press, Boca Raton: 433–481
- Biot MA (1941) General theory of three-dimensional consolidation. *J Appl Phys* 12(2):155–164. <https://doi.org/10.1063/1.1712886>
- Biot MA, Willis DG (1957) The elastic coefficients of the theory of consolidation. *J Appl Mech* 24:594–601. <https://doi.org/10.1115/1.4011606>
- Blaheta R, Kohut R, Kolcun A, Souček K, Staš L, Vavro L (2015) Digital image based numerical micromechanics of geocomposites with application to chemical grouting. *Int J Rock Mech Min Sci* 77:77–88. <https://doi.org/10.1016/j.ijrmm.2015.03.012>
- Buades A, Coll B, Morel J-M (2005) A non-local algorithm for image denoising. In the 2005 IEEE Computer Society Conference on Computer Vision and Pattern Recognition (CVPR'05), San Diego, CA, USA
- Cai Y, Li Q, Liu D, Zhou Y, Lv D (2018) Insights into matrix compressibility of coals by mercury intrusion porosimetry and N<sub>2</sub> adsorption. *Int J Coal Geol* 200:199–212. <https://doi.org/10.1016/j.coal.2018.11.007>
- Chalmers GR, Bustin RM (2007) On the effects of petrographic composition on coalbed methane sorption. *Int J Coal Geol* 69(4):288–304. <https://doi.org/10.1016/j.coal.2006.06.002>
- Chen X, Roshan H, Lv A, Hu M, Regenauer-Lieb K (2020) The dynamic evolution of compaction bands in highly porous carbonates: the role of local heterogeneity for nucleation and propagation. *Prog Earth Planet Sci* 7(1):1–19. <https://doi.org/10.1186/s40645-020-00344-0>
- Chen Y, Zuo J, Liu D, Wang Z (2019) Deformation failure characteristics of coal–rock combined body under uniaxial compression: experimental and numerical investigations. *Bull Eng Geol Env* 78(5):3449–3464. <https://doi.org/10.1007/s10064-018-1336-0>
- Cheng X, Luan H, Chen L, Jiang Y, Han W (2021) Numerical investigation on mechanical properties of inhomogeneous coal under uniaxial compression and the role of cleat distribution. *Bull Eng Geol Env* 80(9):7009–7027. <https://doi.org/10.1007/s10064-021-02357-5>
- Cheng Y, Jiang H, Zhang X, Cui J, Song C, Li X (2017) Effects of coal rank on physicochemical properties of coal and on methane adsorption. *International Journal of Coal Science and Technology* 4(2):129–146. <https://doi.org/10.1007/s40789-017-0161-6>
- Clarkson CR, Bustin RM (1996) Variation in micropore capacity and size distribution with composition in bituminous coal of the Western Canadian Sedimentary Basin: implications for coalbed methane potential. *Fuel* 75(13):1483–1498. [https://doi.org/10.1016/0016-2361\(96\)00142-1](https://doi.org/10.1016/0016-2361(96)00142-1)
- Crosdale PJ, Beamish BB, Valix M (1998) Coalbed methane sorption related to coal composition. *Int J Coal Geol* 35(1–4):147–158. [https://doi.org/10.1016/S0166-5162\(97\)00015-3](https://doi.org/10.1016/S0166-5162(97)00015-3)
- Deng C, Tang D, Liu S, Xu H, Tao S (2015) Characterization of mineral composition and its influence on microstructure and sorption capacity of coal. *J Nat Gas Sci Eng* 25:46–57. <https://doi.org/10.1016/j.jngse.2015.04.034>
- Detheridge A, Hosking LJ, Thomas HR, Sarhosis V, Gwynn-Jones D, Scullion J (2019) Deep seam and minesoil carbon sequestration potential of the South Wales Coalfield, UK. *J Environ Manag* 248:109325. <https://doi.org/10.1016/j.jenvman.2019.109325>
- Detournay E, Cheng AH-D (1993) *Fundamentals of poroelasticity. Analysis and design methods*, Edn. C. Fairhurst. Pergamon Press, Oxford, UK 2:113–171
- Dong H, Zhang Y, Lebedev M, Arif M, Yuan Y, Iglauer S (2021) Simulating Coal Permeability Change as a Function of Effective Stress Using a Microscale Digital Rock Model. *Energy Fuels* 35(10):8756–8762. <https://doi.org/10.1021/acs.energyfuels.1c00619>
- FEI Group (2013) AVIZO 3D Analysis Software
- Franquet J, Abass H (1999) Experimental evaluation of Biot's poroelastic parameter—Three different methods. In the 37th US Symposium on Rock Mechanics (USRMS), Vail, Colorado.
- Gassmann F (1951) Elasticity of porous media. *Vierteljahrsschrift der Naturforschenden Gessellschaft* 96:1–23 ([in German])
- Geertsma J (1957) The effect of fluid pressure decline on volumetric changes of porous rocks. *Transactions of the AIME* 210:331–340. <https://doi.org/10.2118/728-G>
- Golsanami N, Sun J, Liu Y, Yan W, Lianjun C, Jiang L, Dong H, Zong C, Wang H (2019) Distinguishing fractures from matrix pores based on the practical application of rock physics inversion and NMR data: A case study from an unconventional coal reservoir in China. *J Nat Gas Sci Eng* 65:145–167. <https://doi.org/10.1016/j.jngse.2019.03.006>
- Gou S, Li H, Li J, Zhao Y (2021) Effective means to alleviate the greenhouse effect: case study of history match simulations on a brief CO<sub>2</sub> injection into less-deep low-rank coal seams. *Arab J Geosci* 14(9):1–18. <https://doi.org/10.1007/s12517-021-07104-4>
- Guo X, Yao Y, Liu D (2014) Characteristics of coal matrix compressibility: An investigation by mercury intrusion porosimetry. *Energy Fuels* 28(6):3673–3678. <https://doi.org/10.1021/ef5004123>
- Gupta R (2007) Advanced coal characterization: a review. *Energy Fuels* 21(2):451–460. <https://doi.org/10.1021/ef060411m>
- Hou H, Shao L, Li Y, Li Z, Wang S, Zhang W, Wang X (2017) Influence of coal petrology on methane adsorption capacity of the



- Middle Jurassic coal in the Yuqia Coalfield, northern Qaidam Basin, China. *J Petrol Sci Eng* 149:218–227. <https://doi.org/10.1016/j.petrol.2016.10.026>
- Karacan C, Okandan E (2001) Adsorption and gas transport in coal microstructure: investigation and evaluation by quantitative X-ray CT imaging. *Fuel* 80(4):509–520. [https://doi.org/10.1016/S0016-2361\(00\)00112-5](https://doi.org/10.1016/S0016-2361(00)00112-5)
- Karacan CÖ, Ruiz FA, Cotè M, Phipps S (2011) Coal mine methane: A review of capture and utilization practices with benefits to mining safety and to greenhouse gas reduction, *Int J Coal Geol* 86(2–3):121–156. <https://doi.org/10.1016/j.coal.2011.02.009>
- Laxminarayana C, Crosdale P (1999) Role of coal type and rank on methane sorption characteristics of Bowen Basin, Australia coals. *Int J Coal Geol* 40(4):309–325. [https://doi.org/10.1016/S0166-5162\(99\)00005-1](https://doi.org/10.1016/S0166-5162(99)00005-1)
- Li X, Fang Z-M (2014) Current status and technical challenges of CO<sub>2</sub> storage in coal seams and enhanced coalbed methane recovery: an overview. *International Journal of Coal Science & Technology* 1(1):93–102. <https://doi.org/10.1007/s40789-014-0002-9>
- Li Y, Yang J, Pan Z, Tong W (2020) Nanoscale pore structure and mechanical property analysis of coal: An insight combining AFM and SEM images. *Fuel* 260:116352. <https://doi.org/10.1016/j.fuel.2019.116352>
- Liu T, Lin B, Fu X, Liu S (2020) A new approach modeling permeability of mining-disturbed coal based on a conceptual model of equivalent fractured coal. *J Nat Gas Sci Eng* 79:103366. <https://doi.org/10.1016/j.jngse.2020.103366>
- Lv A, Aghighi MA, Masoumi H, Roshan H (2021a) The Effective Stress Coefficient of Coal: A Theoretical and Experimental Investigation. *Rock Mech Rock Eng* 1–17. <https://doi.org/10.1007/s00603-021-02476-1>
- Lv A, Aghighi MA, Masoumi H, Roshan H (2021b) On swelling stress–strain of coal and their interaction with external stress. *Fuel* 122534
- Lv A, Aghighi MA, Masoumi H, Roshan H (2022) The effects of sorbing and non-sorbing gases on ultrasonic wave propagation in fractured coal. *Int J Coal Geol* 249:103906
- Lv A, Ramandi HL, Masoumi H, Saadatfar M, Regenauer-Lieb K, Roshan H (2019) Analytical and experimental investigation of pore pressure induced strain softening around boreholes. *Int J Rock Mech Min Sci* 113:1–10. <https://doi.org/10.1016/j.ijrmm.2018.11.001>
- Mastalerz M, Drobnik A, Strapoć D, Acosta WS, Rupp J (2008) Variations in pore characteristics in high volatile bituminous coals: implications for coal bed gas content. *Int J Coal Geol* 76(3):205–216. <https://doi.org/10.1016/j.coal.2008.07.006>
- Mastalerz M, Gluskoter H, Rupp J (2004) Carbon dioxide and methane sorption in high volatile bituminous coals from Indiana, USA. *Int J Coal Geol* 60(1):43–55. <https://doi.org/10.1016/j.coal.2004.04.001>
- Mathews JP, Campbell QP, Xu H, Halleck P (2017) A review of the application of X-ray computed tomography to the study of coal. *Fuel* 209:10–24. <https://doi.org/10.1016/j.coal.2004.04.001>
- Matsuoka J, Koga T, Suetake N, Uchino E (2017) Robust non-local median filter. *Opt Rev* 24(2):87–96. <https://doi.org/10.1007/s10043-016-0299-2>
- Meng Y, Liu S (2018) Experimental study on sorption induced strain and permeability evolutions and their implications in the anthracite coalbed methane production. *J Petrol Sci Eng* 164:515–522. <https://doi.org/10.1016/j.petrol.2018.01.014>
- Miao Z, Xuehai F, Chaochao D, Yushou L (2020) Influencing factor analysis of the coal matrix compressibility of middle-high rank coals. *J Nat Gas Sci Eng* 81:103462. <https://doi.org/10.1016/j.jngse.2020.103462>
- Pirzada MA, Bahaaddini M, Moradian O, Roshan H (2021) Evolution of contact area and aperture during the shearing process of natural rock fractures. *Eng Geol* 106236. <https://doi.org/10.1016/j.enggeo.2021.106236>
- Pirzada MA, Zoorabadi M, Ramandi HL, Canbulat I, Roshan H (2018) CO<sub>2</sub> sorption induced damage in coals in unconfined and confined stress states: A micrometer to core scale investigation. *Int J Coal Geol* 198:167–176. <https://doi.org/10.1016/j.coal.2018.09.009>
- Pone JDN, Halleck PM, Mathews JP (2009) Sorption capacity and sorption kinetic measurements of CO<sub>2</sub> and CH<sub>4</sub> in confined and unconfined bituminous coal. *Energy Fuels* 23(9):4688–4695. <https://doi.org/10.1021/ef9003158>
- Pone JDN, Halleck PM, Mathews JP (2010) 3D characterization of coal strains induced by compression, carbon dioxide sorption, and desorption at in-situ stress conditions. *Int J Coal Geol* 82(3–4):262–268
- Preim B, Botha CP (2013) Visual computing for medicine: theory, algorithms, and applications. Morgan Kaufmann Publishers Inc, San Francisco, CA, USA
- Ramandi HL, Pirzada MA, Saydam S, Arns C, Roshan H (2021) Digital and experimental rock analysis of proppant injection into naturally fractured coal. *Fuel* 286:119368. <https://doi.org/10.1016/j.fuel.2020.119368>
- Rice JR, Cleary MP (1976) Some basic stress diffusion solutions for fluid-saturated elastic porous media with compressible constituents. *Rev Geophys* 14(2):227–241. <https://doi.org/10.1029/RG014i002p00227>
- Roshan H, Chen X, Pirzada MA, Regenauer-Lieb K (2019a) Permeability measurements during triaxial and direct shear loading using a novel X-ray transparent apparatus: fractured shale examples from Beetaloo basin. *Australia NDT & E International* 107:102129. <https://doi.org/10.1016/j.ndteint.2019.102129>
- Roshan H, Lv A, Xu Y, Masoumi H, Regenauer-Lieb K (2019b) New generation of hoek cells geotechnical testing journal. *Geotech Test J* 42(3):747–760. <https://doi.org/10.1520/GTJ20170110>
- Roslin A, Pokrajac D, Zhou Y (2019) Cleat structure analysis and permeability simulation of coal samples based on micro-computed tomography (micro-CT) and scan electron microscopy (SEM) technology. *Fuel* 254:115579. <https://doi.org/10.1016/j.fuel.2019.05.162>
- Salemi H, Yurikov A, Lebedev M, Behnoudfar P, Rezagholilou A, Iglauer S, Roshan H, Sarmadivaleh M (2021) A novel approach to determine the Biot's coefficient using X-ray computed tomography. *Bull Eng Geol Environ* 80(10):7865–7877
- Shao P, Wang X, Song Y, Li Y (2018) Study on the characteristics of matrix compressibility and its influence factors for different rank coals. *Journal of Natural Gas Science and Engineering* 56:93–106. <https://doi.org/10.1016/j.jngse.2018.05.035>
- Shi JQ, Durucan S (2005) "Gas Storage and Flow in Coalbed Reservoirs: Implementation of a Bidisperse Pore Model for Gas Diffusion in a Coal Matrix." *SPE Res Eval & Eng* 8:169–175. <https://doi.org/10.2118/84342-PA>
- Shi R, Liu J, Wang X, Elsworth D, Liu Z, Wei M, Liu X, Wang Z (2020) Experimental observations of heterogeneous strains inside a dual porosity sample under the influence of gas-sorption: A case study of fractured coal. *Int J Coal Geol* 223:103450. <https://doi.org/10.1016/j.coal.2020.103450>
- Skempton A (1961) Effective Stress in Soils, Concrete and Rocks. *Selected Papers on Soil Mechanics* 1032:4–16
- Song C, Liu S (2020) A novel approach of bulk strength enhancement through microbially-mediated carbonate cementation for mylonitic coal. *Geomicrobiol J* 37(8):726–737. <https://doi.org/10.1080/01490451.2020.1764675>
- Spears D, Caswell S (1986) Mineral matter in coals: cleat minerals and their origin in some coals from the English Midlands. *Int J Coal Geol* 6(2):107–125. [https://doi.org/10.1016/0166-5162\(86\)90015-7](https://doi.org/10.1016/0166-5162(86)90015-7)
- Stappen VJF, Kock DT, Schutter DG, Cnudde V (2019) Uniaxial compressive strength measurements of limestone plugs and

- cores: a size comparison and X-ray CT study. *Bull Eng Geol Env* 78(7):5301–5310. <https://doi.org/10.1007/s10064-018-01448-0>
- Sufian A, Russell AR (2013) Microstructural pore changes and energy dissipation in Gosford sandstone during pre-failure loading using X-ray CT. *Int J Rock Mech Min Sci* 57:119–131
- Tan Y, Pan Z, Feng X-T, Zhang D, Connell LD, Li S (2019) Laboratory characterisation of fracture compressibility for coal and shale gas reservoir rocks: A review. *Int J Coal Geol* 204:1–17. <https://doi.org/10.1016/j.coal.2019.01.010>
- Taylor GH, Teichmüller M, Davis A, Diessel C, Littke R, Robert P (1998) *Organic petrology*, Gebriüder Borntraeger, Stuttgart, Germany
- Terzaghi K (1943) *Theoretical soil mechanics*. John Wiley & Sons, Dordrecht, Netherlands
- Thermo-Fisher-Scientific (2018) *Avizo Software 9 User's Guide*
- Viggiani G, Hall SA (2008) Full-field measurements, a new tool for laboratory experimental geomechanics. In the Fourth symposium on deformation characteristics of geomaterials
- Wang G, Guo Y, Wang P, Li W, Wu M, Sun L, Cao J, Du C (2020) A new experimental apparatus for sudden unloading of gas-bearing coal. *Bull Eng Geol Env* 79(2):857–868. <https://doi.org/10.1007/s10064-019-01601-3>
- Wang G, Jiang C, Shen J, Han D, Qin X (2019a) Deformation and water transport behaviors study of heterogenous coal using CT-based 3D simulation. *Int J Coal Geol* 211:103204. <https://doi.org/10.1016/j.coal.2019.05.011>
- Wang G, Qin X, Han D, Liu Z (2021) Study on seepage and deformation characteristics of coal microstructure by 3D reconstruction of CT images at high temperatures. *Int J Min Sci Technol* 31(2):175–185. <https://doi.org/10.1016/j.ijmst.2020.11.003>
- Wang G, Qin X, Shen J, Zhang Z, Han D, Jiang C (2019b) Quantitative analysis of microscopic structure and gas seepage characteristics of low-rank coal based on CT three-dimensional reconstruction of CT images and fractal theory. *Fuel* 256:115900. <https://doi.org/10.1016/j.fuel.2019.115900>
- Ward CR (1989) Minerals in bituminous coals of the Sydney Basin (Australia) and the Illinois Basin (USA). *Int J Coal Geol* 13(1–4):455–479. [https://doi.org/10.1016/0166-5162\(89\)90104-3](https://doi.org/10.1016/0166-5162(89)90104-3)
- Ward CR (1992) Mineral matter in Triassic and Tertiary low-rank coals from South Australia. *Int J Coal Geol* 20(3–4):185–208. [https://doi.org/10.1016/0166-5162\(92\)90013-M](https://doi.org/10.1016/0166-5162(92)90013-M)
- Wei M-Y, Liu J, Liu Y-K, Liu Z-H, Elsworth D (2021) Effect of adsorption-induced matrix swelling on coal permeability evolution of micro-fracture with the real geometry. *Pet Sci*. <https://doi.org/10.1016/j.petsci.2021.07.006>
- Wetzel M, Kempka T, Kühn M (2018) Quantifying rock weakening due to decreasing calcite mineral content by numerical simulations. *Materials* 11(4):542. <https://doi.org/10.3390/ma11040542>
- Zhang G, Ranjith P, Liang W, Haque A, Perera M, Li D (2019) Stress-dependent fracture porosity and permeability of fractured coal: an in-situ X-ray tomography study. *Int J Coal Geol* 213:103279. <https://doi.org/10.1016/j.coal.2019.103279>
- Zhang L, Yan D, Yang S, Mangi HN, Fu H, Wang G, Yang X, Zhang B, Li T, Liang W (2020) Effects of sequence stratigraphy on coal characteristics and CH<sub>4</sub> adsorption capacity of the low-rank coal in Santanghu Basin, China. *J Nat Gas Sci Eng* 81:103467. <https://doi.org/10.1016/j.jngse.2020.103467>
- Zhang Y, Lebedev M, Al-Yaseri A, Yu H, Xu X, Iglauer S (2018) Characterization of nanoscale rockmechanical properties and microstructures of a Chinese sub-bituminous coal. *J Nat Gas Sci Eng* 52:106–116. <https://doi.org/10.1016/j.jngse.2018.01.037>
- Zhang Y, Zhang Z, Sarmadivaleh M, Lebedev M, Barifcani A, Iglauer S (2017) Prediction of microscale rock mechanical performance from microCT images: heterogeneous coal as an example. In the 51st US Rock Mechanics/Geomechanics Symposium, San Francisco, CA, USA.
- Zhao L (2012) *Mineralogy and geochemistry of Permian coal seams of the Sydney Basin, Australia, and the Songzao Coalfield, SW China*. PhD Dissertation, University of New South Wales.
- Zhao Y, Song H, Liu S, Zhang C, Dou L, Cao A (2019) Mechanical anisotropy of coal with considerations of realistic microstructures and external loading directions. *Int J Rock Mech Min Sci* 116:111–121. <https://doi.org/10.1016/j.ijrmms.2019.03.005>
- Zhao Y, Sun Y, Liu S, Chen Z, Yuan L (2018) Pore structure characterization of coal by synchrotron radiation nano-CT. *Fuel* 215:102–110. <https://doi.org/10.1016/j.fuel.2017.11.014>
- Zhu Q, Song W, Yang Y, Lu X, Liu L, Zhang Y, Sun H, Yao J (2021) An advection-diffusion-mechanical deformation integral model to predict coal matrix methane permeability combining digital rock physics with laboratory measurements. *Appl Geochem* 126:104861. <https://doi.org/10.1016/j.apgeochem.2020.104861>
- Zhu S, Du Z, Li C, You Z, Peng X, Deng P (2018) An analytical model for pore volume compressibility of reservoir rock. *Fuel* 232:543–549. <https://doi.org/10.1016/j.fuel.2018.05.165>
- Zimmerman RW, Somerton WH, King MS (1986) Compressibility of porous rocks. *Journal of Geophysical Research: Solid Earth* 91(B12):12765–12777. <https://doi.org/10.1029/JB091iB12p12765>